Directional Macro–Cell Channel Characterization from Urban Measurements

Alexander Kuchar, Student Member, Jean-Pierre Rossi, and Ernst Bonek, Senior Member

A. Kuchar and E. Bonek are with the Institut für Nachrichtentechnik und Hochfrequenztechnik, Technische Universität Wien, Vienna, Austria. E–mail: Alexander.Kuchar@nt.tuwien.ac.at. E. Bonek is also with the Forschungszentrum Telekommunikation Wien (FTW), A–1040 Wien, Maderstrasse 1. J.-P. Rossi is with France Telecom, CNET/DMR/PMR, 6 avenues des Usines, BP 382, 90000 Belfort, Cedex (F), France. E–mail: jean-pierre.rossi@cnet.francetelecom.fr.

The authors thank A.F. Molisch for a critical reading of the manuscript and H. Bölcskei for his help in the derivation of the data estimation error.

Abstract

We measured the angular power distribution at the mobile station in downtown Paris at 890MHz. The transmit antenna was omnidirectional and placed high above rooftops. The receiver antenna, a 21x41 element rectangular synthetic array, was located on the roof of a van. The refined high–resolution evaluation method, particularly robust against non–stationary signal components, allows an angular resolution of better than 1°, in both azimuth and elevation, and a delay resolution of 33ns.

Combined angular/temporal domain measurements are crucial for the understanding of the propagation mechanisms. The evaluated sites showed strongly street–dominated propagation. We found a combined circular and rectangular distribution of scatterers around the mobile station in street–dominated environments. Propagation over the roofs was significant, typically 65% of energy was incident with elevation larger than 10°. Our results corroborate the hypothesis on the importance of multiple reflections/diffractions in urban macro cells. We explain this behaviour by two reasons: narrow streets favouring a canyon effect and strong scatterers without LOS to the mobile station.

Keywords

Wireless communications, urban channel, channel measurements, direction–of–arrival estimation.

I. Introduction

Future mobile communication systems will use antenna arrays at the base and/or mobile station, either as diversity antennas or as beamforming arrays [1]. For both applications, knowledge of the directional characteristics of the mobile radio channel is crucial for system performance. The availability of proper directional channel models is a prerequisite for the system design and evaluation. Thus the interest in the directional nature of the urban mobile radio channel has rapidly increased over the last years [2], [3].

Directional channel measurements at the *base station* have been reported recently [4], [5]. In the work presented here we measured the angular power distribution at *mobile station* positions. The planar array allowed determination of both the azimuth and the elevation of the incoming waves. The importance of the simultaneous estimation of the two angles is discussed in [6], and it is shown that disregarding the elevation leads to significant error of azimuth estimates. Mutual coupling was avoided by performing measurements with a single antenna that was moved over a rectangular grid. First results of these measurements have been presented in [6]. Here we use a refined evaluation method, which allows a more thorough evaluation with higher sensitivity. The analysis of the complete set of measurements, conducted by CNET France Telecom [7], allowed to propose a classification of environments for urban macro cells. Averaged angular power distributions for these classes are discussed.

Many channel models assume only single reflections. We will investigate the question whether multiple reflected signals at the receiver can be detected and where this is the case. We will also discuss what portion of the signal energy travels over the roofs. To answer this question it is essential to have elevation power distributions at the mobile station position. This information is useful for the description of site–specific deterministic [8] and semi–deterministic channel models [9], [10].

We also study the effect of non–stationary scatterers. The results will support our position that the presented data evaluation method is well suited for the application to measurement data, even if the data is not collected from a strictly stationary channel.

Section II explains the measurement setup and the experimental conditions. Section III reviews the physical model assumptions and Section IV describes the data evaluation procedure. In Section V we present the results of a basic propagation scenario to validate the approach and discuss the influence of non–stationary channel components. Section VI presents an environment classification with representative measurement results for each class. Section VII discusses the averaged angular power distributions. Section VIII concludes the work.

II. Measurement System and Environment

The measurements were performed in downtown Paris. The environment consisted mainly of buildings with heights of about 25–35m. The transmitter was placed on the top of a building in *Rue des Archives*, about 47m above ground level (Fig. 2). The transmit antenna was a 10dBi–gain omnidirectional antenna. As receive antenna we used a quarter wavelength monopole mounted on a conducting shield. It was placed on top of a van at a height of 2m. The antenna was consecutively moved to each node point of a rectangular lattice to form a planar synthetic array, $\vec{r}_m = m_x\Delta_x\,\vec{e}_x + m_y\Delta_y\,\vec{e}_y$ with $0 \leq m_x < M_x$, $0 \leq m_y < M_y$ and $\Delta_x = \Delta_y = 5cm = 0.148\lambda$ (Fig. 1). The array was always aligned with the y–axis parallel to the street ($\phi = 90°$). At each node point, we extract the impulse response by correlating with a replica of the sent pseudo random sequence [11]. The

$M_x \times M_y = 21 \times 41$ impulse responses measured over the "synthetic aperture", $1m \times 2m$, form the spatially variant impulse response

$$\mathbf{h}_{m_x,m_y}(n) \equiv h(\vec{r}_m, n\Delta_\tau), \tag{1}$$

where the delay sampling rate $\Delta_\tau = 0.033\mu s$ with $0 \leq n \leq N = 1023$. This results in a channel impulse response over a delay interval of about $35\mu s$.

Special care was taken to limit the phase errors in the measurements [7], [11]. The transmitter and the receiver were controlled by very precise clocks (Rubidium normal with a drift of $2.10^{-11}/day$). Still the remaining phase shift due to manual clock synchronization would cause significant phase errors. To overcome this difficulty we measured, for *each* antenna position, $\vec{r}_m$, the complex signal at this position and a complex reference signal at a fixed antenna position, $\vec{r}_0$. This allows a correction of the phase shift.

Another source of errors is the possible non–stationarity of the channel between each measurement and its reference measurement. Measuring during the night was important to reduce the main source of non–stationarity, i.e. moving cars. Furthermore the receiver antenna was placed on the roof of a high van on a conducting shield, and thus the influence of surrounding cars was strongly attenuated. However, we discuss the problem of channel non–stationarity in more detail in Sec. V.

III. Physical Assumptions and Definitions

Under the assumption of stationary scatterers in the far–field and the narrow–band assumption [6], the spatially variant impulse response can be written as a sum of L plane waves

$$h(\vec{r}, \tau) \;=\; \sum_{l=1}^{L} \alpha_l e^{j(\vec{k}_l \vec{r})} \delta(\tau - \tau_l). \tag{2}$$

where $\vec{r} = x\,\vec{e}_x + y\,\vec{e}_y$, x and y are the coordinates of the measurement array plane, the wavenumber is $\vec{k}_l = k_{x,l}\vec{e}_x + k_{y,l}\vec{e}_y$, and α_l is the complex amplitude of the l–th wave. The wave vectors are then

$$k_{x,l} = \frac{2\pi}{\lambda_0} \cos\vartheta_l \cos\phi_l, \quad k_{y,l} = \frac{2\pi}{\lambda_0} \cos\vartheta_l \sin\phi_l, \tag{3}$$

where ϕ_l and ϑ_l are the azimuth and the elevation angles of the lth of a total of L incident waves.

A direction–of–arrival (DOA) estimation of h at a given delay τ will give the DOAs of the rays within the delay interval $[\tau - \Delta_\tau, \tau]$, where Δ_τ is the temporal resolution. The number of these rays is usually much smaller than L, and therefore any DOA–determining tool will resolve them more easily.

Further definitions

We define the angle resolved impulse response as

$$\tilde{h}(\phi, \vartheta, \tau) \;=\; \sum_{l=1}^{L} \alpha_l \delta(\phi - \phi_l)\delta(\vartheta - \vartheta_l)\delta(\tau - \tau_l). \tag{4}$$

If a mobile is moving in the direction of the street, $\phi = 90°$, we can transform the angular domain into the normalized Doppler domain, $\nu = sin\phi \; cos\vartheta$, which results in a Doppler–variant impulse response

$$\tilde{h}_\nu(\nu, \tau) \;=\; \sum_{l=1}^{L} \alpha_l \delta(\nu - \nu_l)\delta(\tau - \tau_l). \tag{5}$$

From $\tilde{h}$ and $\tilde{h_\nu}$ we define various power spectra (Tab. I), i.e. sums of powers of the estimated plane waves.

IV. Data Evaluation – Array Processing

The goal of the array processing is to estimate the angle resolved channel impulse response, $\tilde{h}$, from the measured spatially variant channel impulse response, h. In this section we briefly summarize a recently developed technique [6] to evaluate the measurement data. (Alternative methods to estimate the channel parameters are given e.g. in [12], [13].) The refinement of the present paper lies in the selection of the number of DOAs, $\hat{L}_n$. Here we determine $\hat{L}_n$ by looking for a local minimum of the data estimation error (see below). This is an "objective" criterion. In [6] we "manually" determined $\hat{L}_n$ only for those delays with peaks in the PDP that carried the essential signal energy. We now treat the entire PDP as a whole, which results in a more sensitive analysis. In general, more waves now appear albeit weak.

PDP	$P(\tau) = \int_{\vec{r}} \lvert h(\vec{r},\tau)\rvert^2 \, d\vec{r}$
ADPS	$A_\tau(\phi,\tau) = \int_{\vartheta} \lvert\tilde{h}(\phi,\vartheta,\tau)\rvert^2 \, d\vartheta$
APS	$A(\phi) = \int_{\tau}\int_{\vartheta} \lvert\tilde{h}(\phi,\vartheta,\tau)\rvert^2 \, d\vartheta d\tau$
EDPS	$E_\tau(\vartheta,\tau) = \int_{\phi} \lvert\tilde{h}(\phi,\vartheta,\tau)\rvert^2 \, d\phi$
EPS	$E(\vartheta) = \int_{\tau}\int_{\phi} \lvert\tilde{h}(\phi,\vartheta,\tau)\rvert^2 \, d\phi d\tau$
DIR	$D_\tau(\nu,\tau) = \lvert\tilde{h}_\nu(\nu,\tau)\rvert^2$
DPS	$D(\nu) = \int_{\tau} \lvert\tilde{h}_\nu(\nu,\tau)\rvert^2 \, d\tau$

TABLE I

Definition of power spectra. PDP ... power delay profile, ADPS ... azimuth delay power spectrum, APS ... azimuthal power spectrum, EDPS ... elevation delay power spectrum, EPS ... elevation power spectrum, DIR ... Doppler–variant impulse response, DPS ... Doppler power spectrum.

In a first step we write down the $M_x \times M_y$ "snapshots" in a vector

$$\mathbf{x} = [h_{0,0}(n), h_{0,1}(n), \ldots, h_{0,M_y-1}(n), \ldots, h_{M_x-1,M_y-1}(n)]^T, \tag{6}$$

i.e. the $M_x \times M_y$ complex array samples at the delay $\tau_n = n\Delta_\tau$. Next we determine the number of incident waves for each of these vectors $\mathbf{x}$.

The limited amount of data ("single snapshot") does not allow to apply well known statistical criteria [6], [14]. Instead we *a priori* assume a number of DOAs, $\hat{L}_n$, starting with $\hat{L}_n = 1$, and calculate under this assumption the wave parameters:

- We estimate from the single snapshot $\mathbf{x}$ the $\hat{L}_n$ DOAs by applying the high resolution DOA estimation algorithm 2–D Unitary ESPRIT [15] and 2–D spatial smoothing [16]. From the so–found azimuth and elevation angles we can form a steering matrix $\hat{\mathbf{A}}$ ([6], Eq. (11)) and
- reconstruct the individual waves and calculate their complex amplitude vector (beamforming),

$$\hat{\mathbf{e}} = [\alpha_{n,1} \dots \alpha_{n,\hat{L}_n}]^T = \hat{\mathbf{A}}^{+}\mathbf{x}, \tag{7}$$

where $(.)^{+}$ is the Moore-Penrose pseudo inverse [17].

• In the next step we determine a measure for the estimation error of the wave parameters. From the reconstructed amplitude vector $\hat{\mathbf{e}}$ we get an *estimate* of the received data matrix

$$\hat{\mathbf{x}} = \hat{\mathbf{A}}\hat{\mathbf{e}}. \tag{8}$$

A measure for the wave parameter estimation error, the so called "Data Estimation Error", $DEE(\hat{L}_n)$, is defined as

$$DEE(\hat{L}_n) = \frac{||\hat{\mathbf{x}} - \mathbf{x}||_2}{||\mathbf{x}||_2}, \tag{9}$$

where $||.||_2$ denotes the $\mathbb{L}_2$–norm of the vector. To this end, we prove why an appropriately defined data estimation error is a valid measure for the parameter estimation error (see Appendix).

• Then we investigate whether the first local minimum of $DEE(\hat{L}_n)$ or the limit of $\hat{L}_n$, $L_{max} = 48$ [6] is reached. If so, the number of DOAs incident with delay τ_n is $L_n = \hat{L}_n$, otherwise repeat the parameter estimation with an increased $\hat{L}'_n = \hat{L}_n + 1$. Taking the number of DOAs that gives a global minimum of DEE, in general does not yield proper results, because in many cases DEE still decreases if more than the actually present DOAs are assumed. The reason is that additional degrees of freedom are used to model the noise.

After we have repeated the procedure for all *relevant* delays, we obtain an estimate of the directionally resolved impulse response

$$\tilde{h}(\tau, \phi, \vartheta) = \sum_{n=1}^{N} \left(\sum_{l=1}^{L_n} \alpha_{n,l} \delta(\tau - n\Delta_\tau) \delta(\phi - \phi_{n,l}) \delta(\vartheta - \vartheta_{n,l}) \right), \tag{10}$$

where L_n waves arrive with delay $\tau_n = n\Delta_\tau$ at the receiver, and $\phi_{n,l}$, $\vartheta_{n,l}$ are the azimuth and elevation of the l–th wave at corresponding delay. The total number of waves incident is

$$L = \sum_{n=1}^{N} L_n. \tag{11}$$

We decide from the averaged measured impulse response which delays are relevant by applying a threshold a few dB above the noise floor. We estimate the angular power distribution for all delays where the threshold is exceeded. For all other delays $L_n = 0$.

The presented method to estimate the angle resolved impulse response has several advantages:

- Only the number of waves per temporal snapshot is limited by the algorithm, in our case to 48, but not the total number of estimated waves. In our results we estimated up to 1000 waves at each measurement location. This offers the freedom to accommodate as many waves as there are physically present.
- The dynamic range is significantly increased by the large beamforming gain.
- Even if the algorithm gives erroneous estimates of the DOA, the estimation error of the angular resolved impulse response will not increase significantly. For a wave with poor DOA estimates the beamforming will result in negligible amplitudes $\alpha_{n,l}$, because no wave is incident from that direction.

V. Validation

To validate the array processing algorithms and the data extraction procedure we go through two steps: First we verify the method in a simple Line Of Sight (LOS) measurement, and second we investigate the effect of non–stationary/non–coherent signals incident at the receiver by means of computer simulations.

A. LOS scenario

The receiver (Fig. 2, position RX19) was located in a 9m wide street at a distance of 480m from the transmitter (Fig. 3). In the power delay profile (Fig. 4) we can identify one dominant peak that corresponds to the LOS path. Additional weak waves (relative power < -35dB) with larger delay are also present.

Azimuthal delay power spectrum

Figure 5 represents the distribution of the power versus azimuth and delay, i.e. the azimuthal delay power spectrum (ADPS). The figure is read as follows: for each identified wave a peak is plotted in the delay–azimuth plane, where delay (azimuth) corresponds to the radial (azimuthal) coordinate in the plane. An excess delay of zero corresponds to the delay of the first wave incident at the receiver. As in all other measurement locations, the direction of the street is $\phi = 90°$ and is depicted in the map by an arrow (Fig. 2). For the dominant wave we determined $\phi = 88.6°$ and $\vartheta = 4.9°$. The theoretical elevation angle is $\vartheta_{th} = 5.3°$, which we obtained from the RX–TX distance and the TX antenna height. The azimuth angle ϕ_{th} was nearly 90° in our notation, i.e. the direction of the street.

The ADPS reveals that there are some longer–delayed waves coming from the front and less shorter–delayed components from behind. The delay of the significant waves incident from behind ($\phi = 270°$) is smaller because the street ends after $180m$ in that direction. Although the power of the weak components is very small ($-60 \cdots - 40$dB) the sensitive array processing is able to detect those weak signals. Other methods, in general, estimate only the strongest waves.

B. Non–stationarity

A channel that is non–stationary during the measurement period leads to non–coherent signals at the antenna elements. In this subsection, we discuss, by means of synthetically generated data, whether such incoherent waves will disturb the estimation of the wave parameters of stationary signal components.

We investigate how a possibly strong non–stationary signal source will degrade the estimation accuracy of another stationary signal. We thus apply Eqs. (2), (3), with $L = 2$. The first wave originates from a fixed scatterer location denoted by C (carrier). The second wave, the interferer I, represents the non–stationary signal source. As a worst case we added to this wave a random phase term uniformly distributed between 0 and 2π. This additional phase was chosen at random for each antenna element. Equation 2 cannot describe such an incoherent signal and thus it would not make sense to estimate a DOA for it. Additionally we varied the ratio of the signal amplitudes,

$$\alpha_2 = \alpha_1 10^{\frac{C/I}{20}}, \qquad (12)$$

where C/I is the carrier–to–interference ratio of the signal sources. Figure 6 presents the RMS estimation error for the first wave versus C/I. For this worst case scenario the estimation error stays below $1°$ for $C/I > -5dB$. This demonstrates the robustness of the method against non–stationary interfering sources.

VI. Measurement Results

In street dominated environments the incident power is often confined to limited angular ranges. After evaluating 30 measurement locations in urban environment and comparing their angular power distributions we defined three classes: *Street_Classical*, *Street_Corner*, and situations where *Far Echoes* play a significant role. In this section we pick out a representative location for each of these classes. Only two out of 30 locations did not fit the above classifications ("Open Areas").

A. *Street_Classic*

A typical NLOS propagation situation in a street includes:

- short–delayed waves from almost all directions (uniform local scattering around the mobile), and
- longer–delayed waves confined to the directions of the street.

At location RX27 (Fig. 2, position RX27) the receiver was located in *Rue de Rivoli*, a 27m wide street, about 700m away from the transmitter. The PDP (Fig. 7) shows an approximately exponential power decay, which is typical for a scenario where local scatterers dominate the propagation. The delay spread is $S = 1.9\mu s$.

From the ADPS we find that all waves with larger delay are confined to narrow angular ranges in the direction of the street (Fig. 8). Because those dominant directions are not exactly $\phi = 90°$ and $\phi = 270°$ we conjecture that the van was not parked exactly in parallel with the street. The first waves arriving at the MS are incident from more or less all directions (compare Fig. 9), which is typical for local scatterers. At delay $\tau_1 \approx 5.7\mu s$

we identify a strong wave incident from $\phi = 94°$ and $\epsilon = 6.5°$, which is reflected at *Tour St. Jacques* (Fig. 10).

The buildings along the street form a wave-guide ("canyon") in which the waves travel. The waves traveling along the street may have significant delays up to 25μs, which is an indication for multiple scattering. Although the scatterers *near* the mobile station are often assumed to lie only within a circular disk, the ADPS indicates that, in street canyons, the scatterer distribution of *long–delayed* waves has a rectangular shape [22]. Thus the ADPS can be modeled by two superposed distributions: a circular distribution for the short delayed components and a rectangular shaped distribution.

Figure 11 shows the distribution of the elevation of the incoming waves, the EDPS. Propagation over the roofs dominates because 50% of the energy have elevations larger than 16°. The elevation decreases with increasing delay.

The Doppler–variant impulse response summarizes the situation (Fig. 12). For small delays we find a Doppler spectrum with large Doppler spread with more or less uniform shape, typical for scenarios with incoming waves over full half–space [18]. This is in contradiction with the usual assumption of a uniform scatterer distribution in a horizontal plane ([19], [23]). For the large delay the spectrum is dominated by maximum Doppler shift components — typical for street–dominated environments.

A slightly different situation occurs at location RX15 (Fig. 2, position RX15), where the mobile is standing in a narrow street environment with 5m width. The strongest components, and thus the largest amount of energy, are incident from the directions of the street. Additionally we find in the ADPS (Fig. 13) contributions with larger delays from azimuths $\phi \approx 40°$, $\phi \approx 220°$, and $\phi \approx 260°$.

The azimuth–delay–*elevation* function (Fig. 14) shows that the waves incident around $\phi \approx 220°$ are confined to a small elevation range although spread over a many microseconds in delay. Such a situation with same azimuth *and* same elevation, but different delay is a strong indication that the waves have undergone additional scattering before being diffracted over a nearby roof, i.e. they are multiply diffracted/reflected.

B. *Street_Far Echoes*

In some locations the power delay profile at the MS includes strong signal components with large delay, i.e. significant far echoes from large scatterers. If the far scatterer has a LOS to the MS, and thus lies in the direction of the street, the waves will have smaller elevation. More often there is no LOS to the far scatterer (compare also RX30 in [21]). Then the waves will arrive at the receiver by double scattering at least. First they are reflected at the large, far away obstacle and then they are coupled into the street, typically by diffraction on the building roofs or at street corners (compare RX15 in previous subsection).

In location RX24 (Fig. 2, position RX24) we measured a typical bad urban PDP (Fig. 15). The strongest waves have an excess delay of $\tau_1 = 5.9\mu s$ and the delay spread is $S = 1.62\mu\mathrm{s}$. The ADPS (Fig. 16) shows that most of the waves are incident from $\phi = 90°$, the direction of the street.

For small delays local scattering dominates — the Doppler–variant impulse response (Fig. 17) shows a large Doppler spread. At excess delay τ_1 we also find a large Doppler spread, but for all other delays the Doppler spread is small. The EDPS (Fig. 18) gives more insights into the source of those strongest signal components. We identify the two strongest waves with nearly the same power and angles $\phi_1 = 92.1°$, $\vartheta_1 = 0°$, and $\phi_2 = 92.5°$, $\vartheta_2 = 16.9°$. Because wave #1 is incident with elevation $\vartheta = 0°$, we are looking for large obstacles that fit the direction and excess delay.

In the map (Fig. 2) we can identify indeed a significant obstacle that acts as a reflector. The excess delay τ_1 fits to Path A, a reflection at the *Opera de Bastille Paris* with its glass front that is visible from RX24. Waves #1 and #2 traveling the same path in the map differ significantly in elevation only. We assume that wave #2 is first reflected at the Opera, and then is reflected at a grazing angle by a building thus leading to larger elevation but similar azimuth.

C. *Street_Corner*

In contrast to the *Street_Classic* environment, the receiver in RX32 was located near a street crossing close to a church (Fig. 20). The top view of the ADPS (Fig. 21) shows the

wave	delay	power	ϕ	ϑ
	μs	dB	$^\circ$	$^\circ$
#1	0.3	0	236.0	36.0 $^\circ$
#2	0.3	-3.4	63.2	37.2 $^\circ$
#3	0.3	-3.6	280.8	14.5 $^\circ$
#4	1.4	-0.5	86.9	1.3 $^\circ$
#5	1.5	-3.6	269.5	2.4 $^\circ$

TABLE II

Strongest five waves incident at location RX32.

small number of angular ranges that dominate this environment. Investigating the five strongest incident waves (Tab. II) reveals that wave #4 and #5 are traveling along the street, both with small elevation. Wave #1 is diffracted at the street corner or reflected at the church. Wave #3 is incident from the direction of the cut–off street corner (Fig. 20). In the ADPS we find many waves with slightly larger azimuth than wave #3, with delays ranging from $0\mu s$ to $8\mu s$. Here the street corners evidently act as edges at which many waves are diffracted before they finally reach the receiver.

VII. Discussion of Results

We present averaged results of *all* measured locations.

From the distribution of the incident power versus azimuth we find that street canyons force the long–delayed waves to come from the directions of the streets, but street crossings can cause additional signal components. For smaller delays (typically $\tau < 0.4\mu$s) local scatterers, typically uniformly distributed in azimuth, contribute to the power spectra. These nearest scatterers can be modeled to lie within a circular disc. The signal components with larger delay are in general confined to the directions of the street. From the averaged ADPS (Fig. 22) we see that the scatterers are distributed on a rectangle [22]. Here we did not include the locations near street crossings. If the receiver is located near a street crossing, the intersecting streets act as apertures. An ADPS averaged over situations near street crossings (Fig. 23) also includes significant contributions from directions other than $\phi = 90°$ and $\phi = 270°$.

The distribution of the elevation angles has a similar shape in all street dominated environments. Figure 24 shows the averaged EDPS for the environment class *Street*, including *Street_Classic*, *Street_Far Echoes* and *Street_Corner*. A general trend is that the elevation decreases with increasing delay. Especially in streets with homogeneous building height the fast decay of elevation over delay is evident. The averaged EPS (Fig. 25) reveals that the strongest components travel horizontally, while waves travelling over the roofs significantly contribute to the overall signal (on average more than 65% of the energy are incident with elevation $\vartheta > 10°$), even though the pattern of the monopole antenna attenuates waves incident from large elevations.

We also identified waves that are incident from large elevations *and* with large delay (Fig. 14 and Fig. 18). Evidently such echoes can only be explained by multiple reflections/diffractions. Generic situations where multiple reflections may occur are:

- A wave is reflected on a far scatterer that has no LOS to the receiver. From there the wave reaches a roof of a building near the receiver, where it is diffracted and propagates to the receiver.
- A wave travels through a street and is multiply reflected on the walls of the street canyon.

Another indicator for multiple reflections are waves arriving with the *same azimuth* and the *same elevation*, but with different delays (Fig. 14). Evidently the urban environment provides numerous waves that have undergone various delays before reaching a final dominant scatterer that directs them to the receiver.

In the street dominated scenarios we find on average a Doppler spectrum similar to a Jakes spectrum, although waves do not impinge from elevation zero only.

VIII. Conclusions

The evaluation of wideband array measurements at the position of mobiles turned out to be an important tool for understanding the propagation mechanisms in the urban mobile radio channel. Especially the good resolution in delay ($33ns$), and angle (on the order of $1°$) of an improved ESPRIT–based method allows to determine an angle–resolved response consisting of numerous partial waves reaching the mobile station.

The results showed that in street dominated environments the scattering distribution is *not only* circular as assumed by many channel models (e.g. [19], [20]). The distribution of waves with small delay contrasts that with long delay. For small delay, local details in the vicinity of the mobile, e.g. a nearby–parked van and building structures, influence the angular resolved impulse response. In contrast, the signal components with large delay depend more on the global characteristic of the environment, e.g. a strong reflector like a high–rise building. In the metropolitan urban area investigated, we found many scenarios with significant excess delay, while the azimuthal spread was not large. We can model this situation with a rectangular scatterer distribution. From our analysis we conclude that these results are consistent with the canyon effect that favours propagation in narrow angular ranges centered around the street direction. Near street crossings, which present an aperture to the mobile, the situation may be different. Depending on the distance between the mobile and the nearest street crossing, additional directions may appear that are not perpendicular to the street direction.

The elevation of the incident waves made clear that in macro cell environments in NLOS situations propagation over the roof presents a significant portion of the total received energy. We found significant coupling of often multiply reflected/diffracted waves over the roofs into streets.

We have found evidence that waves undergo multiple scattering before being diffracted over nearby roof. This was possible only by the analysis of the *joint* information of delay, azimuth *and* elevation of the incident waves.

The averaged power distributions presented for the various environment classes will allow to validate and configure channel models that include directional components. We will implement the obtained results in our Geometry–based Stochastic Channel Model (GSCM [23], [22]) in a later work.

Appendix

We demonstrate why the data estimation error, DEE, is a measure for the accuracy of the estimate of $\hat{\mathbf{A}}$. Inserting the underlying model $\mathbf{x} = \mathbf{A}\mathbf{e}$ [13] and Eq. (7) in Eq. (9) yields

$$DEE = \frac{||\hat{\mathbf{x}} - \mathbf{x}||_2}{||\mathbf{x}||_2} = \frac{||(\hat{\mathbf{A}}\hat{\mathbf{A}}^+ - \mathbf{I})\mathbf{A}\mathbf{e}||_2}{||\mathbf{x}||_2}. \tag{13}$$

Using $||(\hat{\mathbf{A}}\hat{\mathbf{A}}^+ - \mathbf{I})\mathbf{A}\mathbf{e}||_2 \leq ||(\hat{\mathbf{A}}\hat{\mathbf{A}}^+ - \mathbf{I})\mathbf{A}||_2 ||\mathbf{e}||_2$, we obtain

$$DEE \leq \frac{||(\hat{\mathbf{A}}\hat{\mathbf{A}}^+ - \mathbf{I})\mathbf{A}||_2 ||\mathbf{e}||_2}{||\mathbf{x}||_2}, \tag{14}$$

which shows that DEE will be small indeed if $\hat{\mathbf{A}} \approx \mathbf{A}$. This follows from the fact that $\mathbf{P} = \hat{\mathbf{A}}\hat{\mathbf{A}}^+ - \mathbf{I}$ is the projection onto the null space of $\hat{\mathbf{A}}$, which in turn is the null space of $\mathbf{A}$ for $\hat{\mathbf{A}} = \mathbf{A}$. Using the orthogonality of the range space of $\mathbf{A}$ and the null space of $\mathbf{A}$ establishes that DEE is a measure for the quality of the estimate of $\hat{\mathbf{A}}$.

References

[1] J. H. Winters, *Smart Antennas for Wireless Systems*, IEEE Personal Communications Magazine, February 1998, pp. 23–27.

[2] R. B. Ertel, P. Cardieri, K. W. Sowerby, T. S. Rappaport, and J. H. Reed, *Overview of Spatial Channel Models for Antenna Array Communication Systems*, IEEE Personal Communications Magazine, February 1998, pp. 10–22.

[3] U. Martin, J. Fuhl, I. Gaspard, M. Haardt, A. Kuchar, C. Math, A.F. Molisch, and R. Thomä, *Model Scenarios for Direction-Selective Adaptive Antennas in Cellular Mobile Communication Systems - Scanning the Literature*, Wireless Personal Communications 11, Special Issue on SDMA, 1999, pp. 109–129.

[4] K.I. Pedersen, P.E. Mogensen, and P.H. Fleury, *Power Azimuth Spectrum in Outdoor Environments*, IEE Electronic Letters, vol. 33, no. 81, August 1997, pp. 1583–1584.

[5] U. Martin, *Spatio–Temporal Radio Channel Characteristics in Urban Macrocells*, IEE Proc.–Radar, Sonar Navigation, vol. 145, no. 1, February 1998, pp. 42–49.

[6] J. Fuhl, J.-P. Rossi, and E. Bonek, *High-Resolution 3-D Direction–of–Arrival Determination for Urban Mobile Radio*, IEEE Trans. on Antennas and Propagation, vol. AP–45, no.4, April 1997, pp. 672–682.

[7] A. J. Levy, *Fine structures of the urban mobile propagation channel*, in Proc. Commsphere 1991, Herzliya, Israel, Dec. 1991, pp. 5.1.1–5.1.6.

[8] K. Rizk, R. Valenzuela, and F. Gardiol, *Lateral, Full–3D and Vertical Plane Propagation in Microcells and Small Cells*, in Proc. 48th IEEE Veh. Technol. Conf., VTC'98, Ottawa, Cananda, May, 1998.

[9] *COST 231: Urban Transmission Loss Models for Mobile Radio in the 900 and 1800MHz Bands (Revision 2)*, in COST 231 TD(90) 119 Rev. 2, Den Haag, September 1991.

[10] E. Damosso and L. M. Correia (ed.), *Digital Mobile Communications —The View of COST 231*, Commission of the European Union, Luxemburg, 1999.

[11] A. J. Levy, J.-P. Rossi, J.-P. Bardot, and J. Martin, *An improved channel sounding technique applied to wideband mobile 900 MHz propagation measurements*, in Proc. 40th IEEE Veh. Technol. Conf., VTC'90, Orlando, FL, May 7–10, 1990, pp. 513–519.

[12] B. Fleury, D. Dahlhaus, R. Heddergott, and M. Tschudin, *Wideband Angle of Arrival Estimation Using the SAGE Algorithm*, in IEEE Conference Proc. ISSTA'96, Mainz, Germany, pp. 79–85.

[13] C. Brunner, M. Haardt, and J.A. Nossek, *Efficient High–Resolution 3–D Channel Sounding to Determine Realistic Directional Simulation Models for Smart Antennas*, in *Proc.ITG–Diskussionssitzung*, Kaiserslautern, Dec. 1997.

[14] M. Wax and T. Kailath, *Detection of Signals by Information Theoretic Criteria*, IEEE Trans. on Acoustics, Speech, and Signal Processing, vol. ASSP–33, no. 2, April 1985.

[15] M.D. Zoltowski, M. Haardt, and C.P. Mathews, *Closed–Form 2–D Angle Estimation with Rectangular Arrays in Element Space of Beamspace via Unitary ESPRIT*, IEEE Trans. on Signal Processing, vol. 44, no. 2, Feb. 1996, pp. 316–328.

[16] T.-J. Shan, M. Wax, and T. Kailath, *On Spatial Smoothing for Direction–of–Arrival Estimation of Coherent Signals*, IEEE Trans. on Acoustics, Speech, and Signal Processing, vol. ASSP–33, no. 4, August 1985, pp. 806–811.

[17] G. H. Golub and C. F. van Loam, *Matrix Computations*, Baltimore, MD: John Hopkins Univ. Press, 1983.

[18] R. H. Clarke and W. L. Khoo, *3–D Mobile Radio Channel Statistics*, IEEE Trans. Vehicular Technology, vol. 46, 1997.

[19] W.C.Y. Lee, *Effects on Correlation between Two Mobile Radio Base Station Antennas*, IEEE Trans. on Communications, vol. 21, Nov. 1973, pp. 1214–1224.

[20] J.J. Blanz and P. Jung, *A Flexible Configurable Spatial Model for Mobile Radio Channels*, IEEE Trans. on Communications, vol. 46, no. 3, March 1998, pp. 367–371.

[21] A. Kuchar, E. Aguilera Aparicio, J.-P. Rossi, and E. Bonek, *Azimuth, Elevation, and Delay of Signals at Mobile Station Site*, Virginia Tech Symposium on Wireless Personal Communications 1998, June 10-12 1998, Blacksburg (VA), pp.99 - 110.

[22] A.F. Molisch, J. Laurila, A. Kuchar, and R. Schmalenberger, *Test scenarios for mobile radio systems with adaptive antennas*, Proc. ITG Fachtagung "Wellenausbreitung bei Funksystemen und Mikrowellensystemen", Oberpfaffenhofen, Germany, 11.-13. May 98, 1998, see also
A.F. Molisch, A. Kuchar, J. Laurila, K. Hugl, and R. Schmalenberger, *Geometry–based directional model for mobile radio channels — principles and implementation*, submitted to ETT European Transactions on Telecommunications.

[23] J. Fuhl, A.F. Molisch, and E. Bonek, *A Unified Channel Model for Mobile Radio Systems with Smart Antennas*, IEE Proc.–Radar, Sonar Navigation, vol. 145, no. 1, February 1998, pp. 32–41.

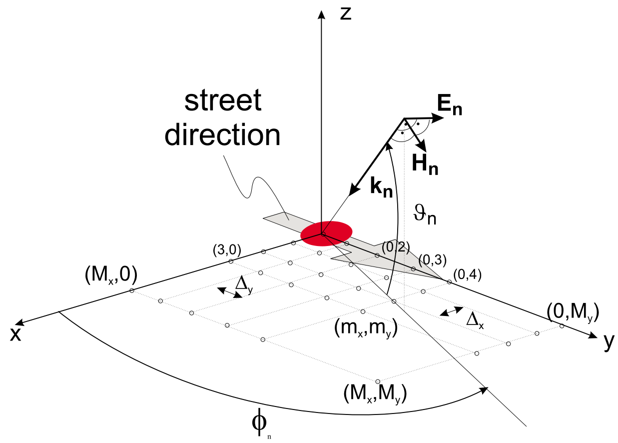

Fig. 1. Definition of the geometrical parameters.

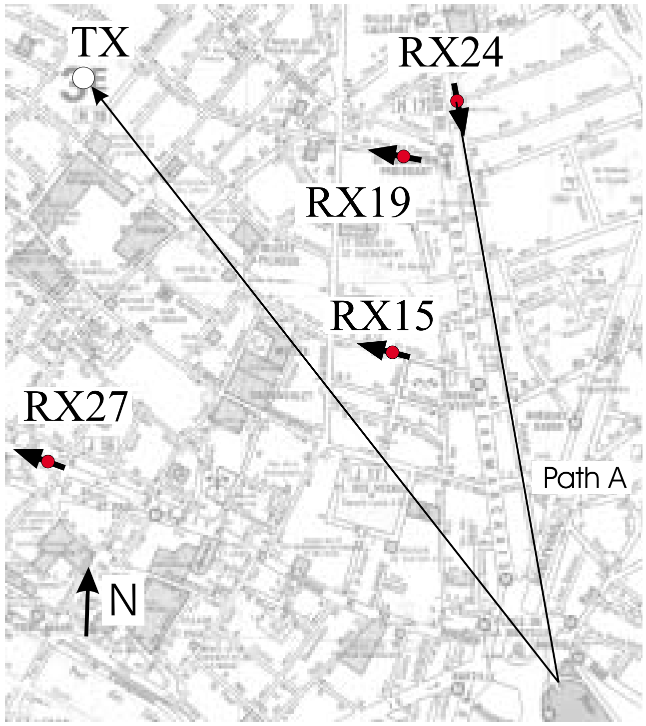

Fig. 2. Map of the measurement locations RX15, RX19, RX24, and RX27. TX indicates the transmitter location. The arrows in the map indicate the receiver orientation ($\phi = 90°$). In contrast to all other locations, RX19 was in LOS to the transmitter. In RX15 and RX24 the receiver was located in a narrow street, in RX27 the receiver was located in a broad, long street.

Fig. 3. Photo taken at position RX19 with view to the transmitter.

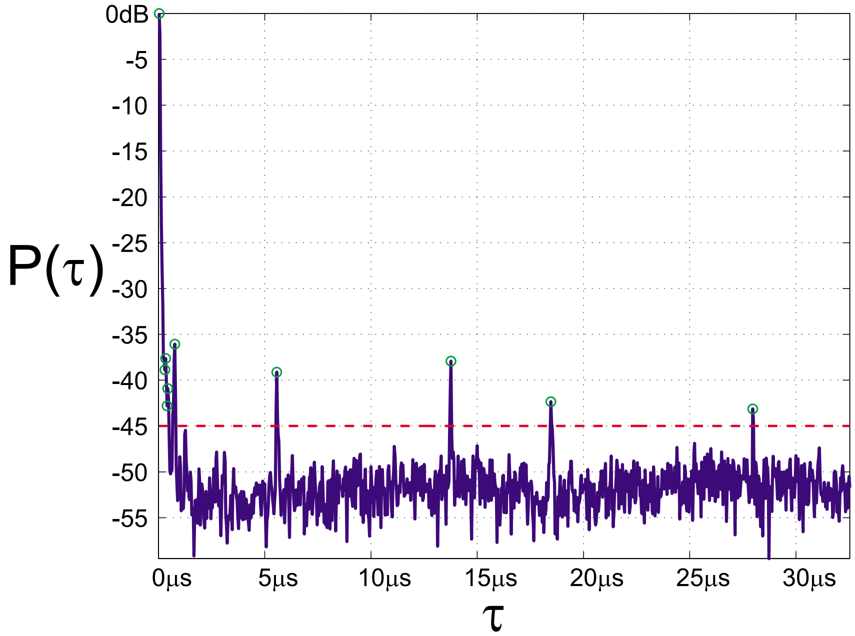

Fig. 4. PDP, $P(\tau)$, of the incoming waves at measurement location RX19 with LOS to the base station.

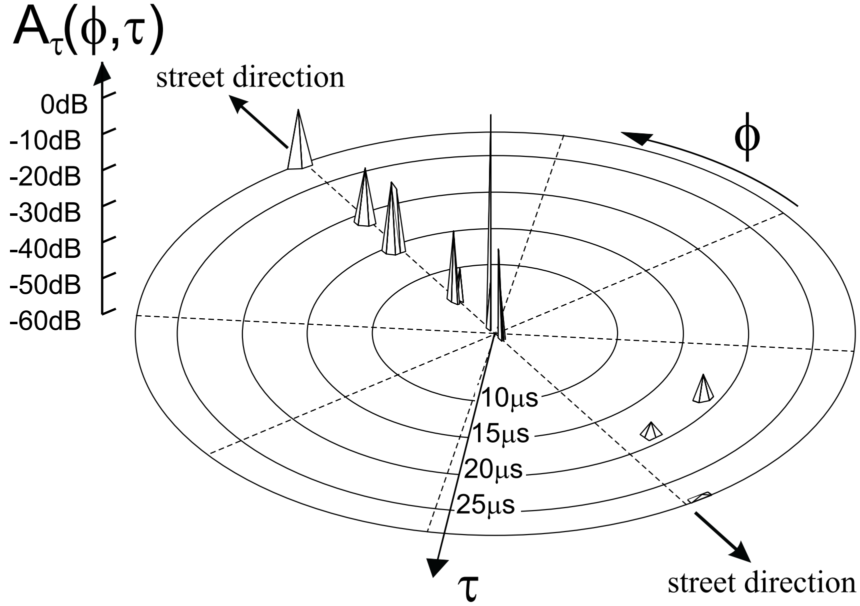

Fig. 5. Azimuthal delay power spectrum (ADPS), $A_\tau(\phi,\tau)$, of the incoming waves for the measurement location RX19 with LOS to the base station.

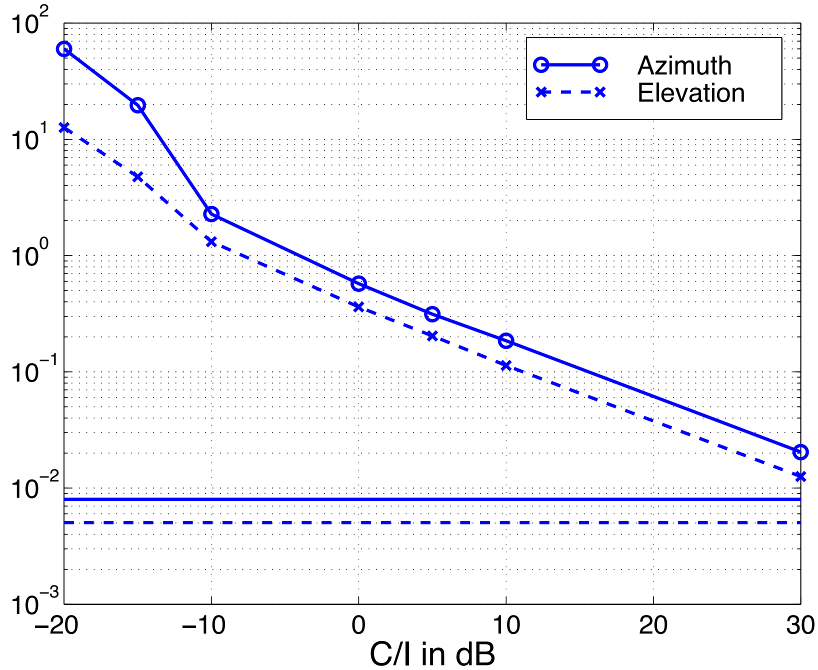

Fig. 6. RMS azimuthal (solid line, circles) and elevation (solid line, crosses) estimation error of a stationary signal source, when a non–stationary interferer source is present. The lines without markers represent the RMS estimation errors of azimuth (solid) and elevation (dashed) when no interferer is present, i.e. $C/I = \infty$.

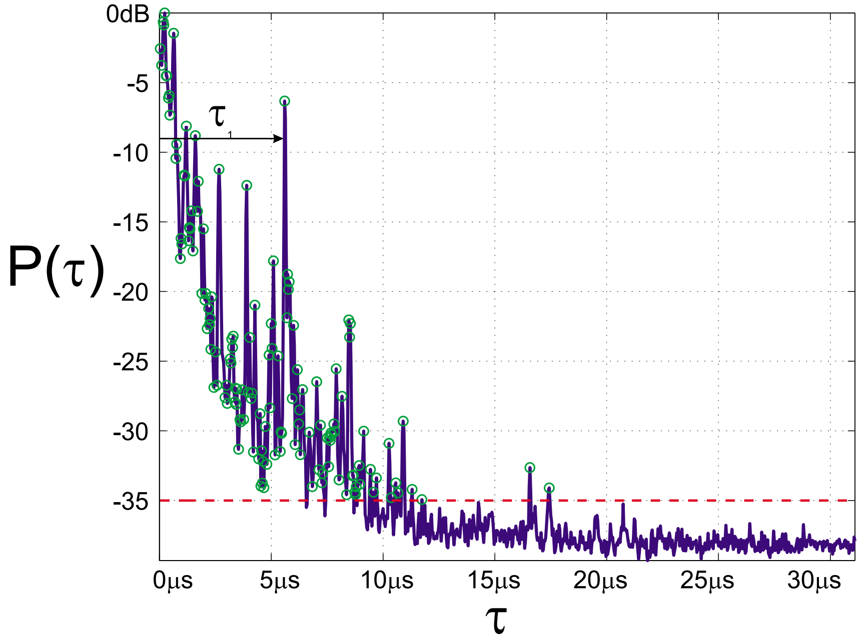

Fig. 7. PDP, $P(\tau)$, of the incoming waves for the measurement location RX27 located in a street.

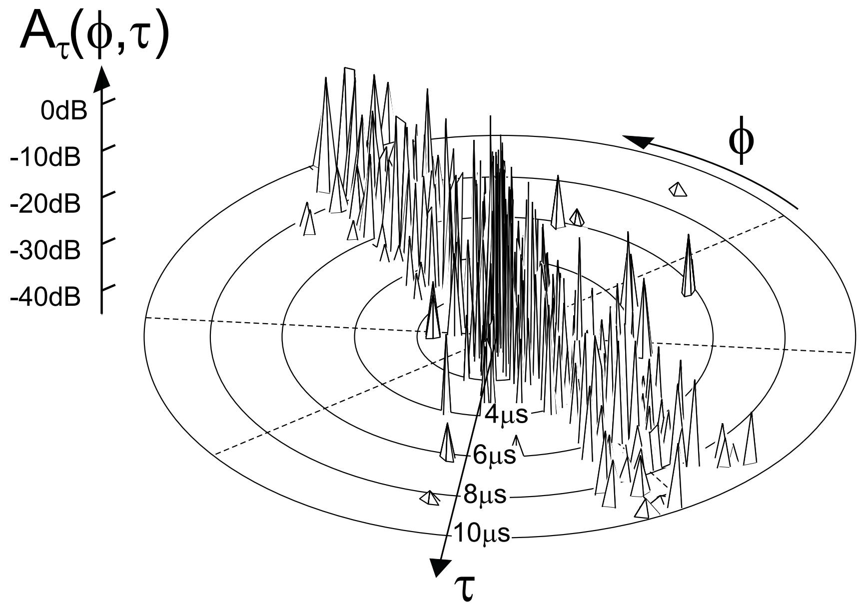

Fig. 8. ADPS, $A_\tau(\phi, \tau)$, of the incoming waves for the measurement location RX27. The waves with large delay are confined to angular ranges in the direction of the street.

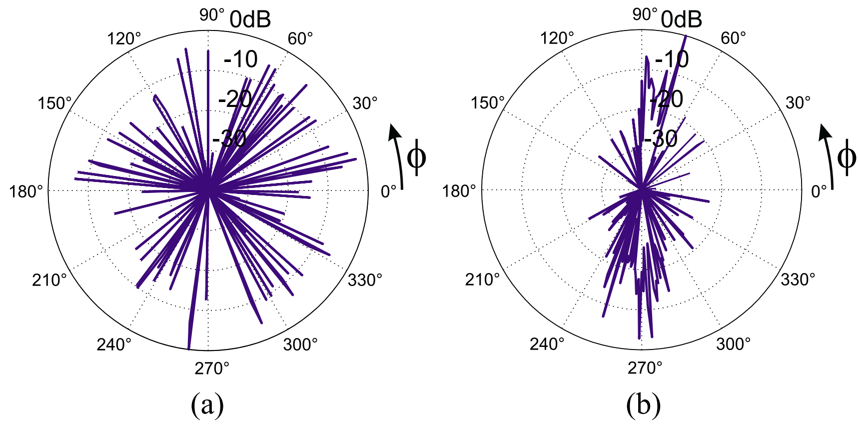

Fig. 9. Normalized APS, $A(\phi)$, of the incoming waves for the measurement location RX27. We separately calculated an APS for small and large delays. The APS plotted on the left side includes all waves with an excess delay $\tau \leq 0.4\mu s$, while in the other APS only waves with an excess delay $\tau > 0.4\mu s$ are included. Waves with small delay are incident from all directions. The canyon effect forces waves with large delay to come mainly from the directions of the street.

Fig. 10. Photo taken at position RX27 with view to the east (Rue de Rivoli).

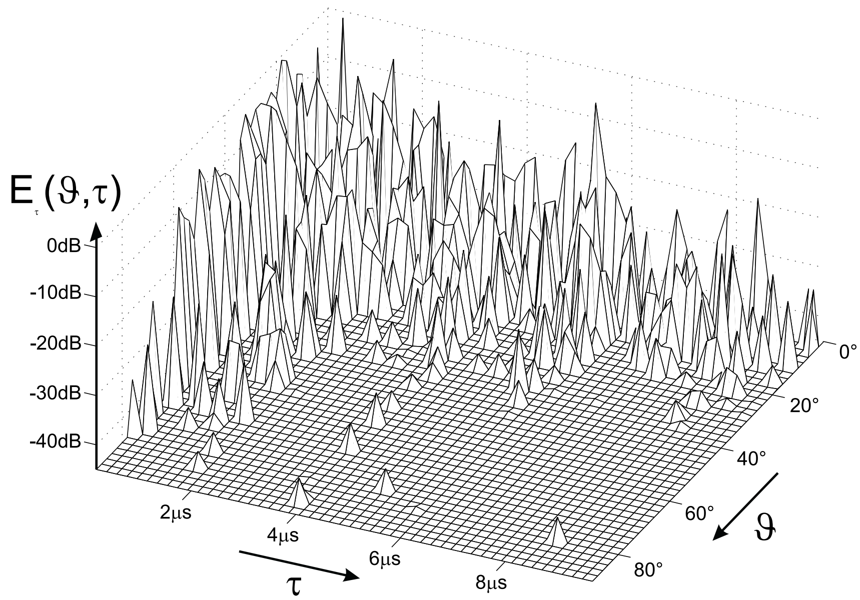

Fig. 11. EDPS, $E_\tau(\vartheta, \tau)$, of the incoming waves for the measurement location RX27. Elevation angles up to 80° are possible especially for the zero excess delay. The elevation decreases with increasing delay.

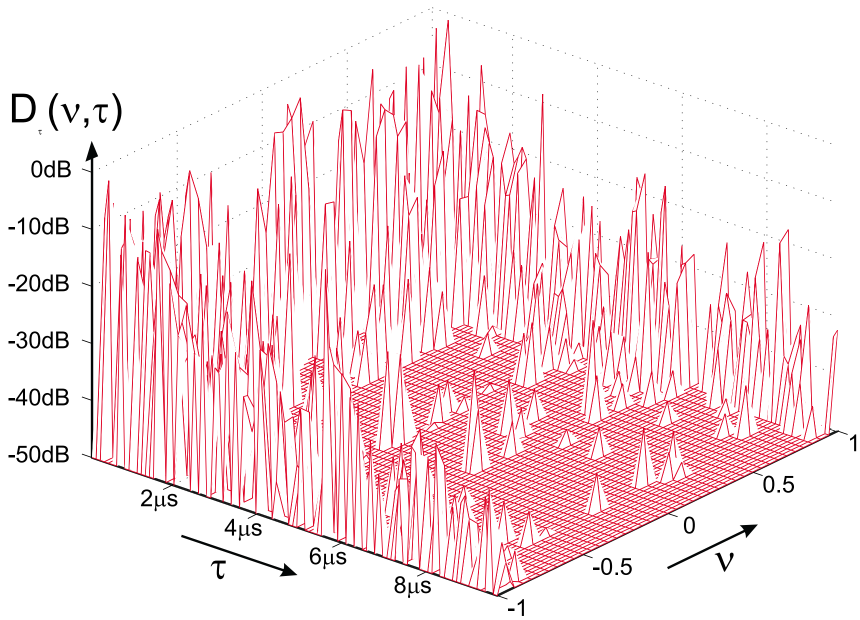

Fig. 12. Doppler–variant impulse response, $D_\tau(\nu, \tau)$, of the incoming waves for the measurement location RX27.

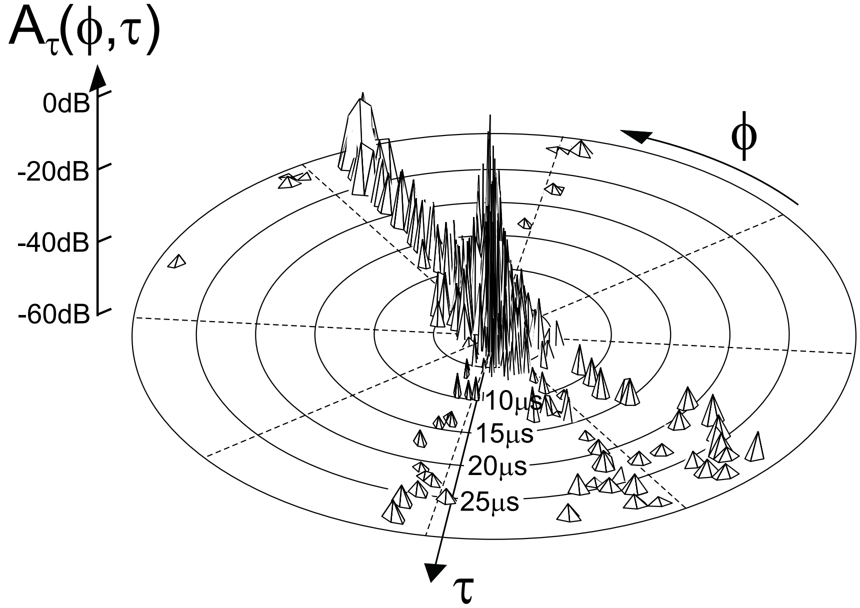

Fig. 13. ADPS, $A_\tau(\phi, \tau)$, of the incoming waves for the measurement location RX15.

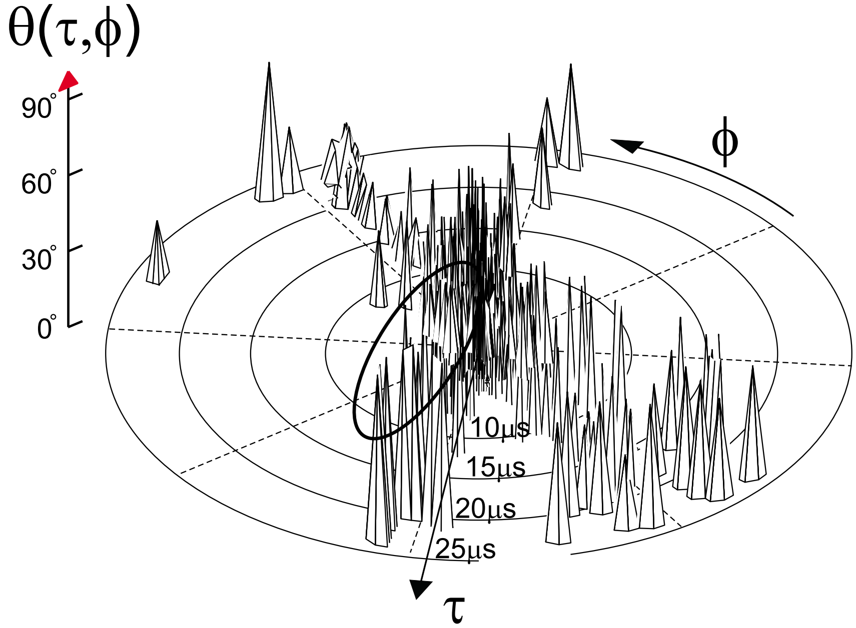

Fig. 14. Elevation over azimuth–delay plane of the incoming waves for the measurement location RX15. Waves that propagate horizontally, i.e. with $\vartheta = 0$, are suppressed in this diagram. Typically, waves incident from other directions than the street have larger elevation. Especially waves near azimuth $\phi = 220°$ (marked) have large and similar elevation (see text).

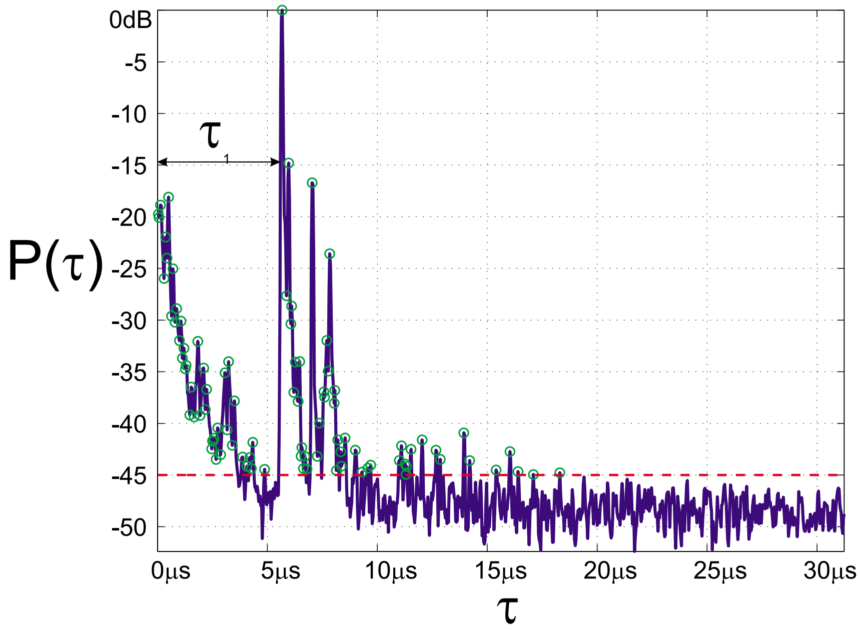

Fig. 15. PDP, $P(\tau)$, of the incoming waves for the measurement location RX24. The delay spread is $S = 1.62\mu s$.

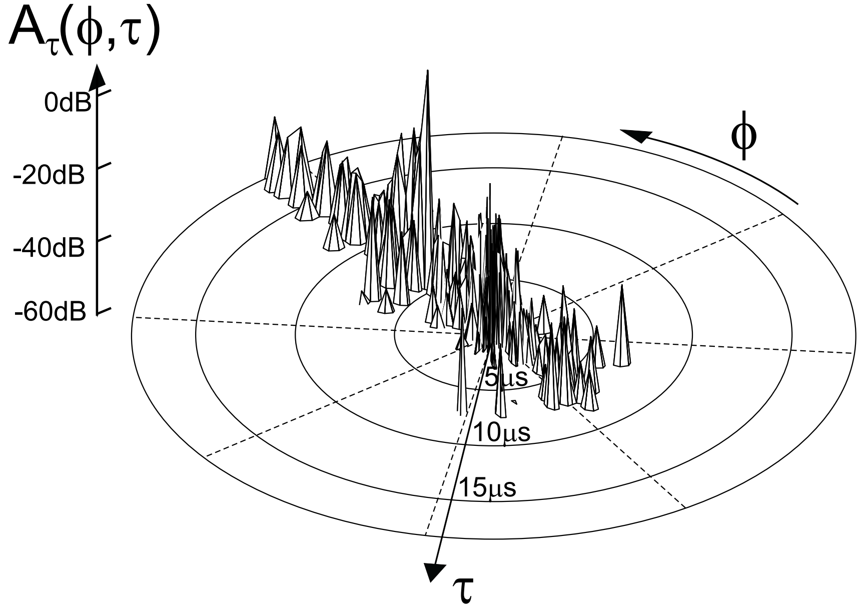

Fig. 16. ADPS, $A_\tau(\phi, \tau)$, of the incoming waves for the measurement location RX24. The strongest wave is incident from the direction of the street, $\phi = 90°$.

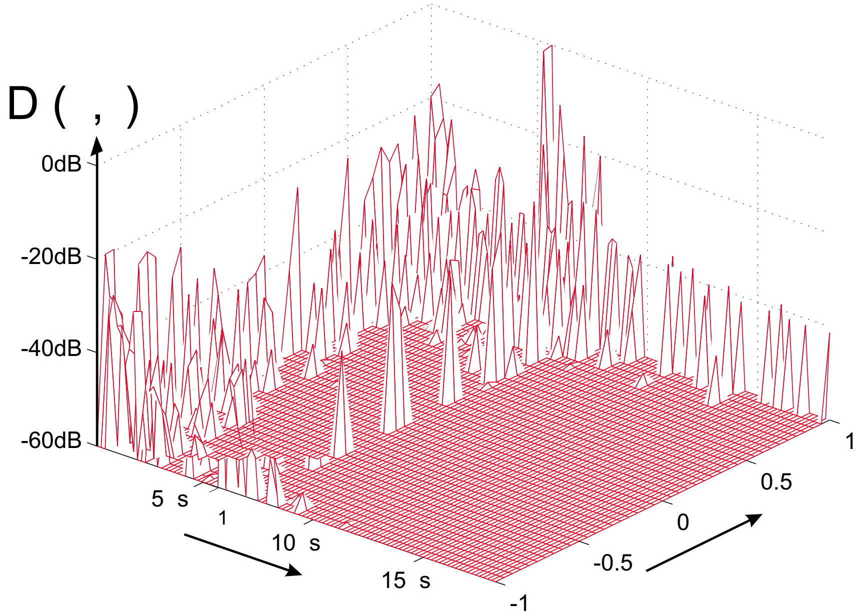

Fig. 17. Doppler–variant impulse response, $D_\tau(\nu, \tau)$, of the incoming waves for the measurement location RX24.

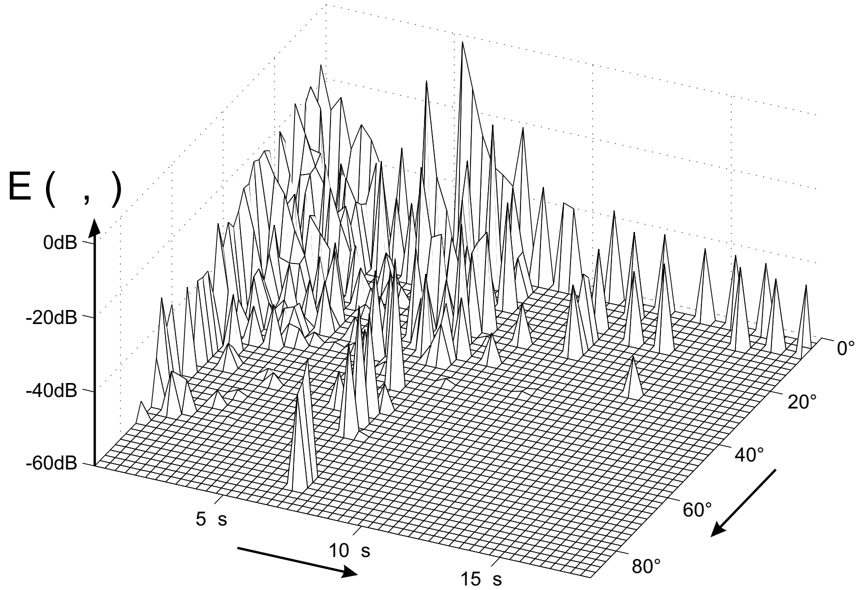

Fig. 18. EDPS, $E_\tau(\vartheta, \tau)$, of the incoming waves for the measurement location RX24.

Fig. 19. Photo taken at position RX24 with view to the south.

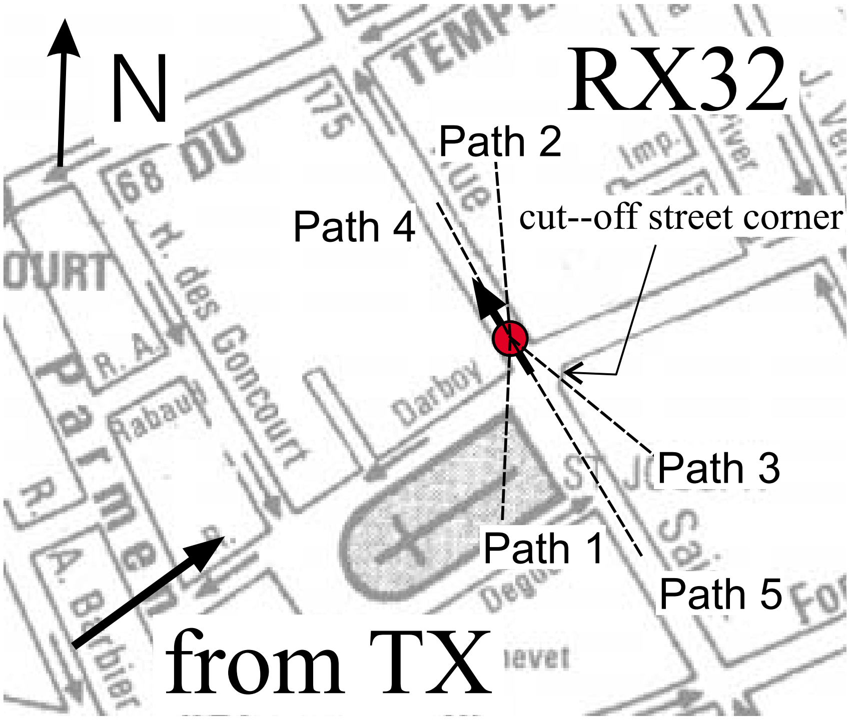

Fig. 20. Measurement location RX32 near a street corner.

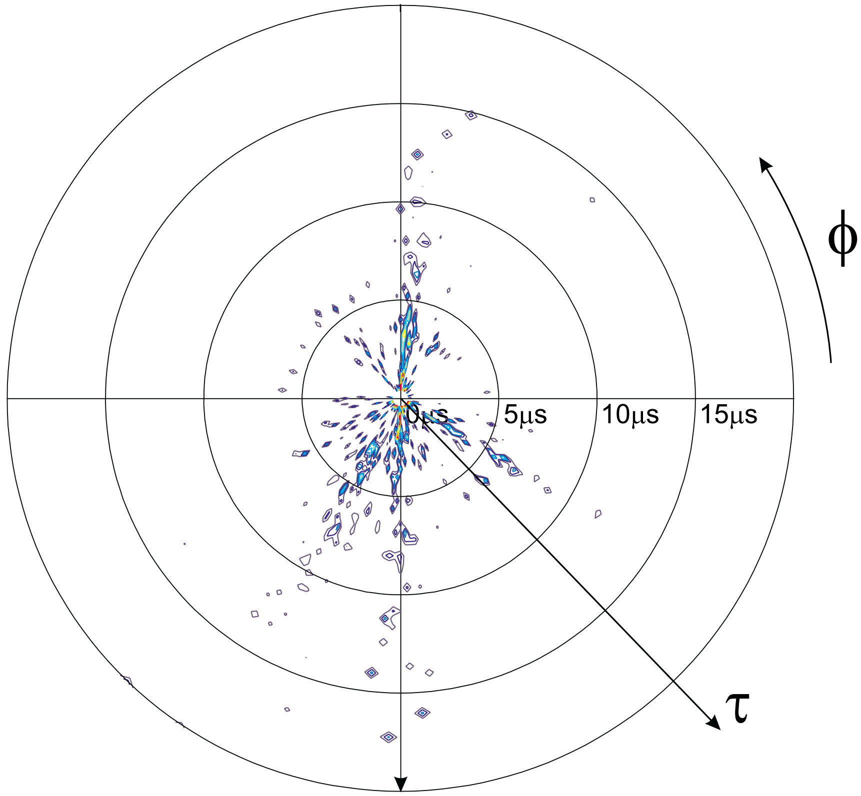

Fig. 21. Top view of the ADPS, $A_\tau(\phi, \tau)$, of the incoming waves for the measurement location RX32 near a street corner.

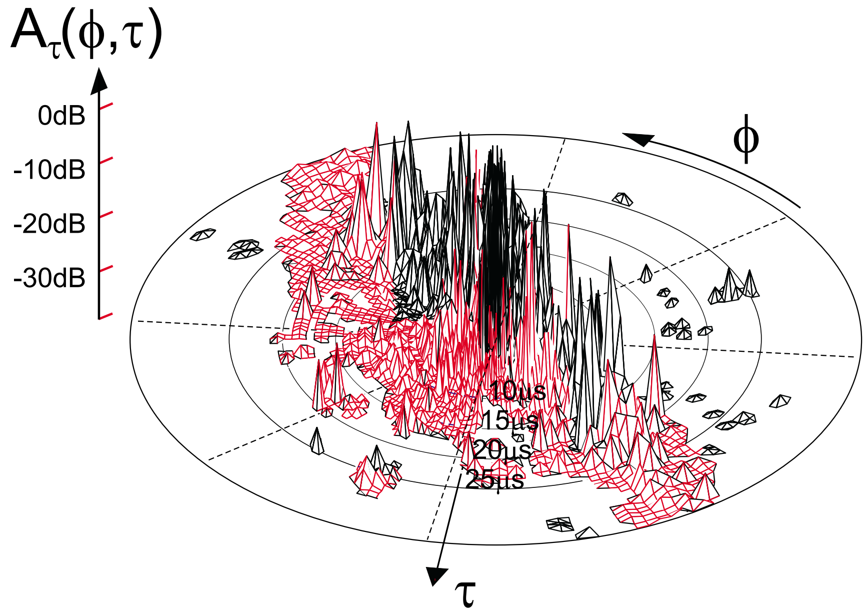

Fig. 22. Averaged ADPS, $A_\tau(\phi, \tau)$, of the incoming waves. We averaged over all scenarios in street environments, including the environment classes *Street_Classic* and *Street_Far Echoes*.

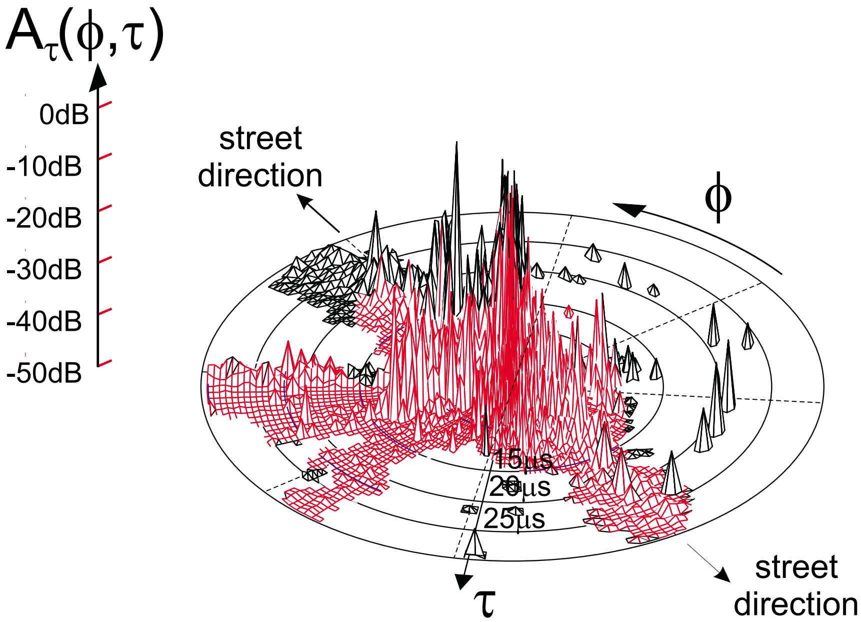

Fig. 23. Averaged ADPS, $A_\tau(\phi, \tau)$, of the incoming waves. We averaged over all scenarios in the environment class *Street_Corner*.

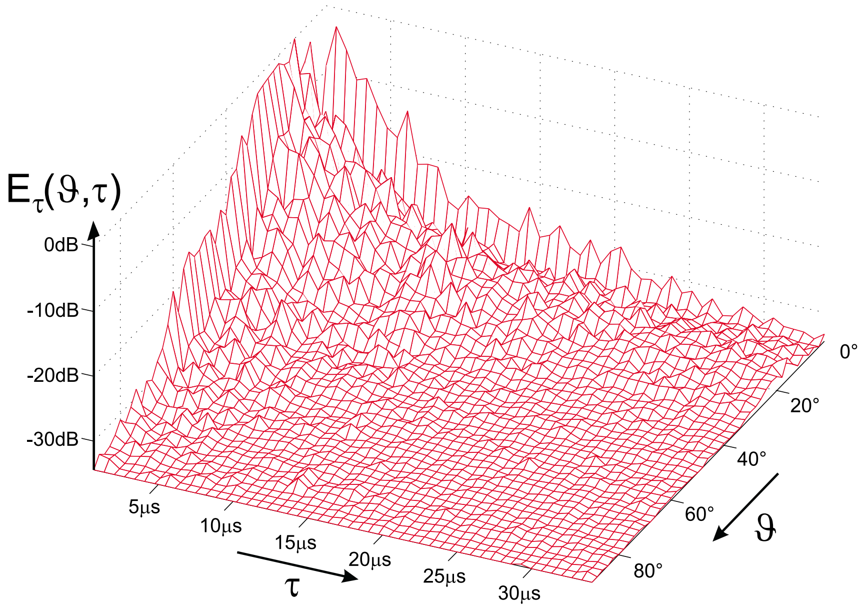

Fig. 24. Averaged EDPS, $E_\tau(\vartheta, \tau)$, of the incoming waves. We averaged over all scenarios in street environments, including the environment classes *Street_Classic*, *Street_Far Echoes*, and *Street_Corner*.

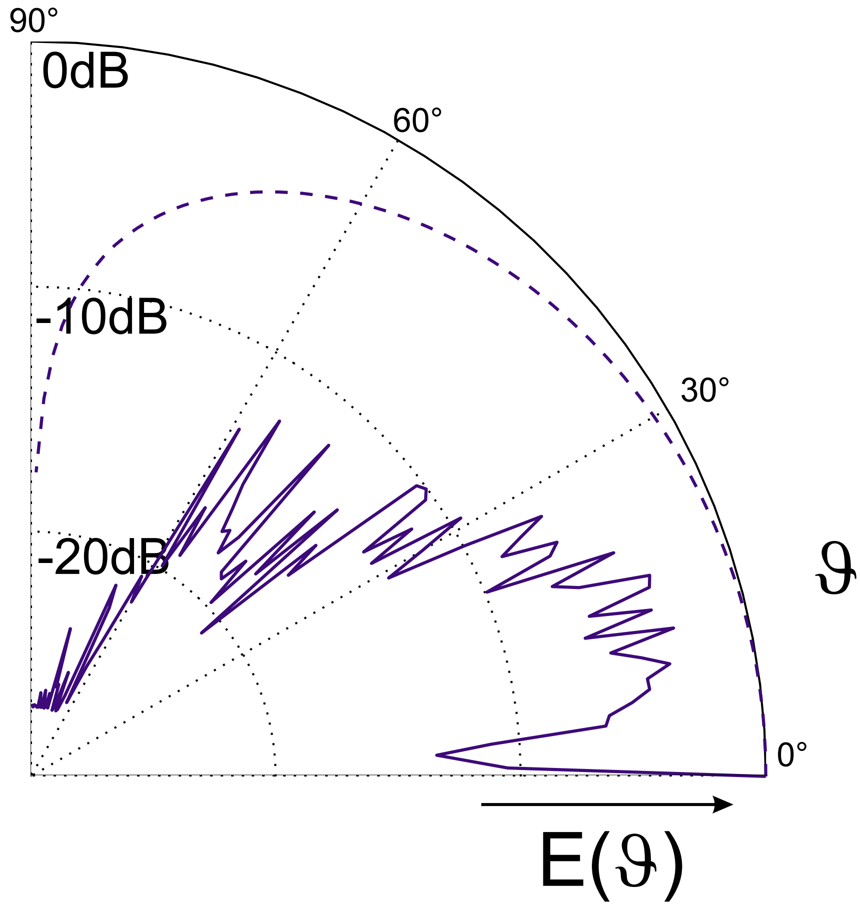

Fig. 25. Averaged EPS, $E(\vartheta)$, of the incoming waves (solid line). We averaged over all scenarios in street environments, including the environment classes *Street_Classic*, *Street_Far Echoes*, and *Street_Corner*. The dashed line represents the vertical antenna pattern of a $\lambda/4$ monopole mounted on a infinite conducting plane.

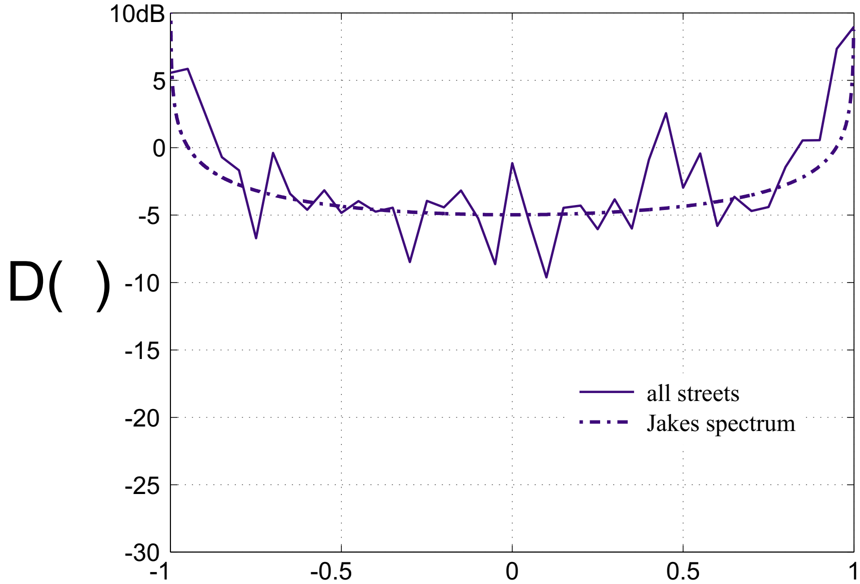

Fig. 26. Averaged Doppler–variant impulse response, $D(\nu)$, of all street–dominated locations. solid line ... *Street*, dash–dotted ... theoretical Jakes spectrum.

List of Figures

Alexander Kuchar (S'96) Alexander Kuchar was born in Vienna, Austria, in 1971. He received the Dipl.–Ing. degree (with highest honors) in electrical engineering from the Technische Universität Wien, Vienna, Austria, in 1996. He is currently finishing his PhD at the Institut für Nachrichtentechnik und Hochfrequenztechnik of Technische Universität Wien, where he is a member of the Mobile Communciations Group. His main research interests are in signal processing for smart antennas for mobile communication systems, directional channel modeling, and microstrip antenna arrays.

Jean–Pierre Rossi Jean–Pierre Rossi was born in Marseille (France) on October 29, 1959. He completed his PhD in 1988 at the laboratory of electromagnetics and applied mathematics of the university Aix–Marseille III. He joined the CNET (Centre National d'Etudes des Télécommunications) in October 1988 to study UHF radio–communication channel. A particular interest was paid to ray theory and its implementation in urban environment. Since march 1995, he is in charge of a research group on physical modelling for radio–mobile propagation in the same company.

Ernst Bonek (M'73, SM'85) Ernst Bonek was born 1942 in Vienna, Austria. He received the Dipl.–Ing. and Dr.techn. degrees (with highest honors) from the Technische Universität Wien (TU Wien). In 1984, he was appointed Full Professor of Radio Frequency Engineering at the TU Wien. His field of interest is mobile communications at large. Recent contributions concern smart antennas, the characterization of mobile radio channels, cordless telephony, and advanced antennas and receiver designs. Altogether, he authored or co–authored some 100 journal publications. He holds four patents, and six more applications on mobile radio technology are pending.

From 1985 to 1990, he served the IEEE Austria Section as a Chairman. From 1991 to 1994 he was a council member of the Austrian Science Fund, acting as speaker for engineering sciences. From 1996 to 1999 he served on the Board of Directors of the reorganized Post and Telekom Austria. He participates in the European research initiative COST 259 as chairman of the working group on Antennas and Propagation. In URSI, he is presently chairman of Commission C "Signals and Systems". He is an Area Editor of "Wireless Personal Communications".